12th International Symposium on Turbulence and Shear Flow Phenomena (TSFP12)
Osaka, Japan, July 19–22, 2022

ON THE ORIGIN OF SECONDARY FLOWS IN TURBULENT BOUNDARY LAYERS OVER ROUGH WALLS

Ioannis K. Kaminaris, Elias Balaras,
Department of Mechanical and Aerospace Engineering
The George Washington University
Washington, DC, USA
kaminaris@gwu.edu; balaras@gwu.edu

Ralph J. Volino and Michael P. Schultz
United States Naval Academy
Annapolis, MD, USA
volino@usna.edu; mschultz@usna.edu

ABSTRACT

Boundary layers with irregular roughness generate and sustain mean-flow heterogeneities in a cross-stream plane, which manifest as high and low momentum pathways in the mean streamwise velocity. Herein, to investigate their origin and evolution we report direct numerical simulations of a turbulent boundary layer with a zero pressure gradient evolving over truncated cones in staggered and random configurations. A correlation of the momentum pathways with the topographical statistics is detected and mainly attributed to the *leading-edge* of the roughness and the strong presence of highly clustered areas throughout the roughness domain. The high and low momentum pathways are present on both staggered and random topographies, but are much weaker and confined near the roughness crest in the former case. In the random cases they depart from the wall and approach the outer edge of the boundary layer.

Introduction

In recent years several studies have focused on the presence of secondary flows over rough-wall boundary layers, which are mean flow features observed in the cross-stream plane perpendicular to the dominant flow direction and have long been studied in non-circular ducts. However, their origin and correlation to the roughness topography remain open questions. Initially it was generally accepted that topographies with regular roughness arrangements generate stronger secondary flows when compared to topographies with irregular arrangements. Mejia-Alvarez & Christensen (2013) showed evidence of secondary flows over irregular topographies, which were directly associated to regions with mean streamwise momentum deficit or low momentum pathways (LMP), and regions with mean streamwise momentum surplus or high momentum pathways (HMP). In a followup study, Barros & Christensen (2014) correlated the spanwise locations of the LMP with recessed topography, and those of the HMP with elevated topography. Recently Womack *et al.* (2022) conducted an experimental study over regular and irregular topographies and observed secondary motions similar to those of Mejia-Alvarez & Christensen (2013) for the case of random arrangements. They found no correlation, however, between the locations of the momentum pathways and the local topography. Instead they noted that a correlation may exist with the leading part of the roughness.

In the present study Direct Numerical Simulations (DNS) of a turbulent boundary layer with zero pressure gradient over a rough wall are presented. Roughness is generated by staggered and random arrangements of truncated cones. The roughness geometries and parametric space are identical to the ones utilized in the experiments reported by Womack *et al.* (2022). The latter is also used to validate the DNS. The study aims to address some of the remaining questions about the nature and the origin of secondary flows over rough walls. Emphasis is given on their correlation to the topographical statistics. The impact of the secondary motions on the flow statistics is also discussed.

Methodologies and parametric space

Following Womack *et al.* (2022) the rough surface was created utilizing truncated cones in random and staggered configurations, which resemble barnacles found on fouled ship hulls. For the staggered arrangement a coverage level of 39% (S39) is considered, while for the random we will report three coverage levels: 10% (R10), 39% (R39) and 57% (R57). The computational domain was also designed to match the experiment and is shown in Figure 1: the boundary layer develops over a flat plate of $200D \times 28D$, in the streamwise (x) and spanwise (z) directions respectively (D is the base diameter of the truncated cone) and the freestream boundary is positioned $20D$ from the wall. The inflow boundary is positioned upstream of the rough area to allow the boundary layer to develop over the smooth portion first. A turbulent boundary layer with zero pressure gradient matching the experiment is specified as an inflow boundary condition which is extracted from an earlier computation over a smooth wall. The Reynolds number at the inflow plane is set to $Re_\theta = U_\infty \theta_o / \nu = 1600$ ($\theta_o = 0.16D$ is the momentum thickness at the inflow plane, U_∞ the freestream velocity and ν the kinematic viscosity of the fluid). The domain is discretized using $6000 \times 1200 \times 350$ grid points in the streamwise (x), wall-normal (y) and spanwise (z)

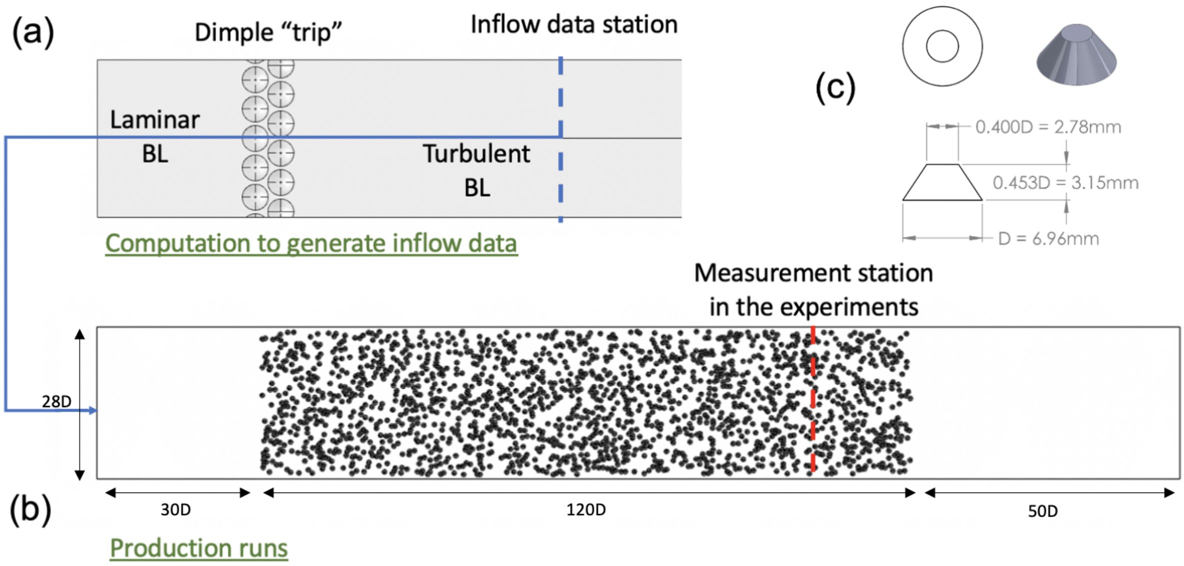

Figure 1: Computational setup corresponding to the experiments reported byWomack *et al.* (2022). (a) Precursor simulation to generate inflow boundary conditions; (b) Computational domain used for all production runs; (c) Truncated cones used to generate all topographies.

directions respectively, resulting in $\Delta x^+ = 11$, $\Delta y^+ = 1.9$ and $\Delta z^+ = 9.3$ (based on the average friction velocity u_τ for the smooth part of the plate. Each barnacle is discretized by approximately $36 \times 42 \times 67$ points in the streamwise, spanwise and wall-normal directions respectively.

The roughness elements were immersed in the Cartesian grid and the non-slip condition was enforced using an immersed boundary formulation. In particular, an in-house, finite-difference, Navier–Stokes solver is utilized for all cases presented in this work. All spatial derivatives are discretized using second-order central differences on a staggered gird. Equations are advanced in time with a semi-implicit fractional step method. A direct-forcing, immersed-boundary method is used to impose the no-slip condition on the roughness elements. The details on the overall formulation can be found in Yang & Balaras (2006).

Results

All computations were initialized using smooth-wall data and were advanced in time until the effects of the initial conditions were washed out. Time averaged statistics were accumulated over four flow-through times for all cases. We found this sample size to be a good compromise between convergence and cost. To validate the DNS we compare the mean velocity profiles and velocity fluctuations to the experimental measurements. Comparisons are done at the streamwise location ($x/D = 103$ from the leading edge of the roughness) where the experimental measurements by Womack *et al.* (2022) are reported. Figure 2 shows the mean velocity profiles for the two random arrangements: R10 and R57. Outer coordinates are used to eliminate uncertainties coming from the computation of the wall stress. The agreements with the experiments is very good. Figure 3 shows the corresponding velocity fluctuations $\overline{u'u'}$, $\overline{v'v'}$ in the streamwise and wall-normal directions respectively. Also in this case the agreement to the experiments is good and the observed discrepancies are within the uncertainty of the measurements and the statistical sampling error in the simulations.

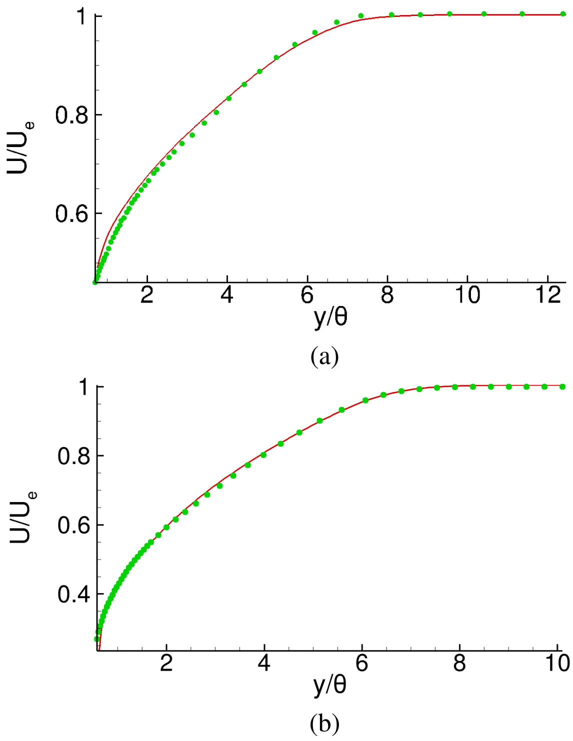

Figure 2: Mean streamwise velocity profiles at $x/D = 103$ in outer coordinates ——— DNS; • experiment by Womack *et al.* (2022). (a) random topography, R10; (b) random topography, R57.

Having established confidence in the DNS results, next we conducted detailed analysis of the secondary flow patterns

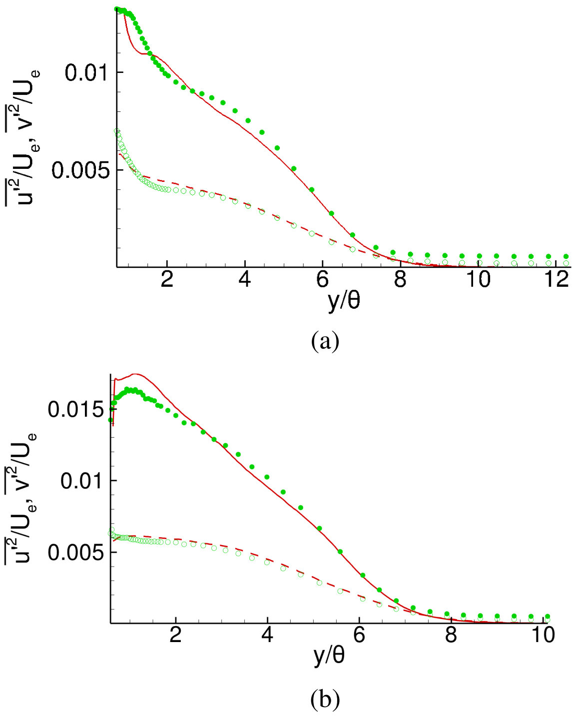

Figure 3: Normal Reynolds stress profiles at $x/D = 103$ in outer coordinates. ——— $\overline{u'u'}$, - - - $\overline{v'v'}$, • $\overline{u'u'}$, ○ $\overline{v'v'}$; Lines are from the DNS and symbols from the experiment by Womack *et al.* (2022). (a) random topography, R10; (b) random topography, R57.

that may be present in this class of flows. In the experimental work by Mejia-Alvarez & Christensen (2013) and Womack *et al.* (2022), for example, secondary flows were observed in the cross-stream plane at the measurement station, and their impact on the momentum transport was clearly visible on the "bending" of the mean streamwise velocity isolines on the plane. This essentially generates "channeling" of the mean flow in alternating high and low momentum areas, typically called HMP and LMP respectively. These are mean flows features and to visualize them one can plot the fluctuations of the time averaged streamwise velocity in the spanwise direction:

$$\tilde{u} = \overline{u} - < \overline{u} >_z, \tag{1}$$

where $\bar{\cdot}$ is the time averaging operator and $< . >_z$ is the spanwise averaging operator. Areas of $\tilde{u} > 0$ correspond to HMP and of $\tilde{u} < 0$ to LMP. In Figure 4 a top view of isosurfaces of $\tilde{u}/U_e \sim \pm 5\%$ are shown for two cases of staggered (S10) and random (R39) arrangements. The momentum pathways detected over the staggered arrangement (Figure 4a) are very weak and confined to the roughness crest throughout the boundary layer evolution. This may also be the reason that they have not been detected in the experiments by Womack *et al.* (2022), as the first measurement point is typically above the roughness crest. For the random cases, on the other hand, HMP and LMP are very coherent and occupy over the full extent of the plate in the streamwise direction (Figure 4b). Clearly most of these structures originate directly from the leading edge of the roughness and remain fairly coherent in the streamwise direction. These observations are in agreement with the findings of Womack *et al.* (2022), where they also observed strong secondary flows throughout the boundary layer in the random arrangements and none in the case of the staggered arrangements.

Close inspection of the the evolution of the HMP/LMP in the boundary layer revealed that at their origin (i.e. the leading edge of the roughness) they are located very close to the roughness elements, while as one moves downstream they grow, lift-off the wall and occupy a substantial part of the boundary layer. A three-dimensional view of the secondary flows and related momentum pathways is shown in Figure 5, where the mean cross-plane vectors normalised by their magnitude and colored by the mean streamwise vorticity, alongside with momentum pathways at a region close the experimental measurement location ($x/D = 103$) are plotted. It can be seen that strong, streamwise coherent counter-rotating secondary flows are present on both sides of the HMP base accounting for the lateral momentum transfer: high momentum fluid is laterally transferred from the HMP regions to the core of the LMP. The counter-rotation of the secondary flows is demonstrated by the sign difference in the streamwise vorticity, consistent with the spanwise alternation of the HMP and LMP. Similar behaviour was observed in all random arrangements with different percentage coverage. For the staggered case (not shown here for simplicity) the counter-rotating secondary flow motions followed the topography and were confined below the roughness crest.

The origin of the momentum pathways and hence of the secondary flows is still an open question. Barros & Christensen (2014) suggested that the LMP and HMP correlate with the local recessed and elevated roughness, respectively. Womack *et al.* (2022), however, found no correlation between the momentum pathways and the local topography and presented evidence that these structures may originate from leading edge of the roughness. To investigate this conjecture utilizing the DNS database we first need to quantify the correlation between the topography and HMP/LMP. To capture a representative sample of the surface we define sample volumes that cover the rough surface and have a streamwise and spanwise length of $\sim 3\overline{d}_{min}$ (where $\overline{d}_{min}$ is mean minimum distance to neighbor roughness elements), and varying height (i.e. 2 to 20 times the roughness height, k) depending of their streamwise location in order to overlap with the HMP/LMP in the boundary layer. Within each volume we compute averaged local topographical statistics, as well as an average of $\tilde{u}/U_e$, which depending on the sign indicates the presence of a low or high momentum pathway. Their correlation is reported at a particular streamwise location where consecutive volumes are arranged along the spanwise direction. Figure 6, for example demonstrates the relation between the local topography and presence of HMP/LMP. The latter is captured by the frontal area coverage, λ_f, which is computed as follows:

$$S_f = \begin{cases} \vec{n_u} \cdot \vec{S}, & \vec{n_u} \cdot \vec{n_s} < 0 \\ 0, & \vec{n_u} \cdot \vec{n_s} \geq 0 \end{cases}, \quad where \;\; n_s = \vec{S} / \left\| \vec{S} \right\|. \tag{2}$$

Note n_s is the surface unit vector, n_u is the unit vector in the direction of the mean flow (i.e. x-direction) and $\vec{S}$ the surface area vector. The frontal area coverage, λ_f, is then computed by:

$$\lambda_f = \frac{S_f}{S_o} 100\%, \quad where \;\; S_o = \vec{n_o} \cdot \vec{S}, \tag{3}$$

and n_o is the unit vector in the wall-normal direction. Figure 6a,c shows the relation between λ_f and the momentum

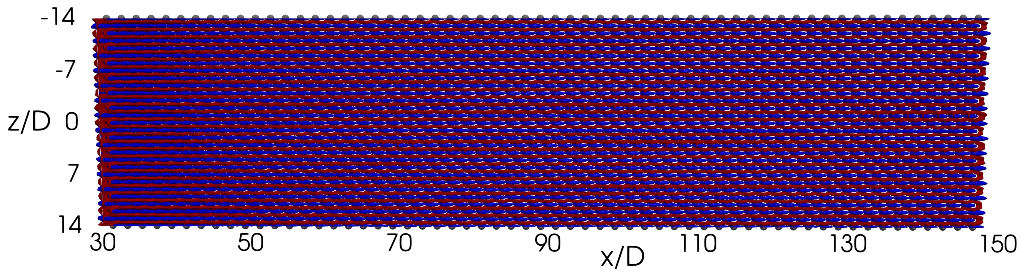

(a)

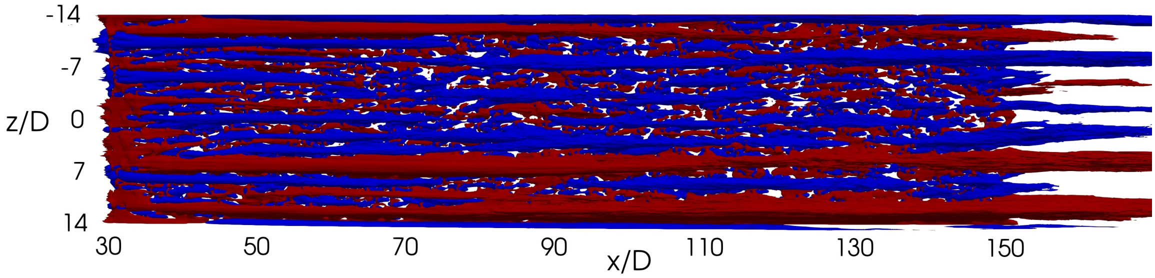

(b)

Figure 4: Top view of HMP/LMP visualized by isosurfaces of $\tilde{u}$: —— $\tilde{u}/U_e = 5\%$ HMP; —— $\tilde{u}/U_e = -5\%$ LMP. (a) staggered arrangement S39; (b) random arrangement R39.

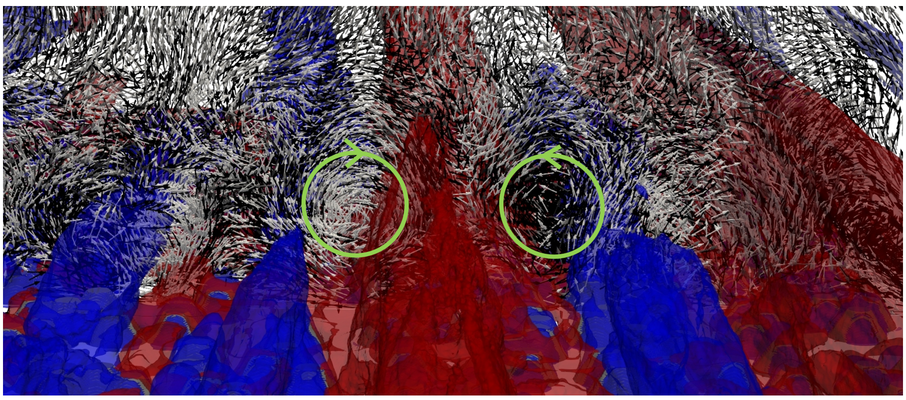

Figure 5: Three dimensional view of the mean cross-plane velocity vectors in the vicinity of HMP and LMP (also shown as isosurfaces) for the case of the random arrangement, R39. Velocity vectors are normalised by magnitude and colored by the streamwise vorticity. Green circles mark the counter-rotating vortices.

pathways (captured by $\pm\widetilde{u}$) at the leading edge of the roughness for both random cases considered: R10 and R57. It is clear that high positive values of $\widetilde{u}$, representative of HMP, are only present in areas where $\lambda_f = 0$. Large negative values of $\widetilde{u}$, representative of LMP on the other hand, are only present in areas of large λ_f. The high levels of correlation between the topography and momentum pathways are the leading edge are not presnet further downstream. Figure 6b,d shows the same quantities further downstream at $x/D = 103$. No such correlation is observed and LMP can be found in non-clustered or lower frontal area coverage areas. The same applies to HMP that are also found in high frontal area coverage areas. This result supports the conjecture that HMP/LMP, at least for this particular family of roughness topographies, are generated at the leading edge of the roughness and remain coherent for several boundary layer thicknesses downstream. In addition, the downstream topography just underneath does not significantly affect their evolution.

To further investigate the role of the leading edge topography on the structure of the momentum pathways over the whole roughness patch we conducted several numerical experiments around the R39 case and: i) changed the distribution of λ_f along the spanwise direction at the leading edge of the roughness by rearranging the truncated cones over a small strip while keeping the coverage the same (the topography further downstream remained unchanged); ii) removed all roughness elements downstream of the leading edge (see Figure 7c). In the former case (not shown here) the locations of HMP/LMP shifted to coincide with the new distribution of λ_f and established a similar correlation with the one demonstrated in Figure 6a,c. A visualization of HMP/LMP for both cases is shown in Figure 7. Despite the elimination of the downstream roughness, the momentum pathways are still formed and their original spanwise locations are preserved. It is noted that al-

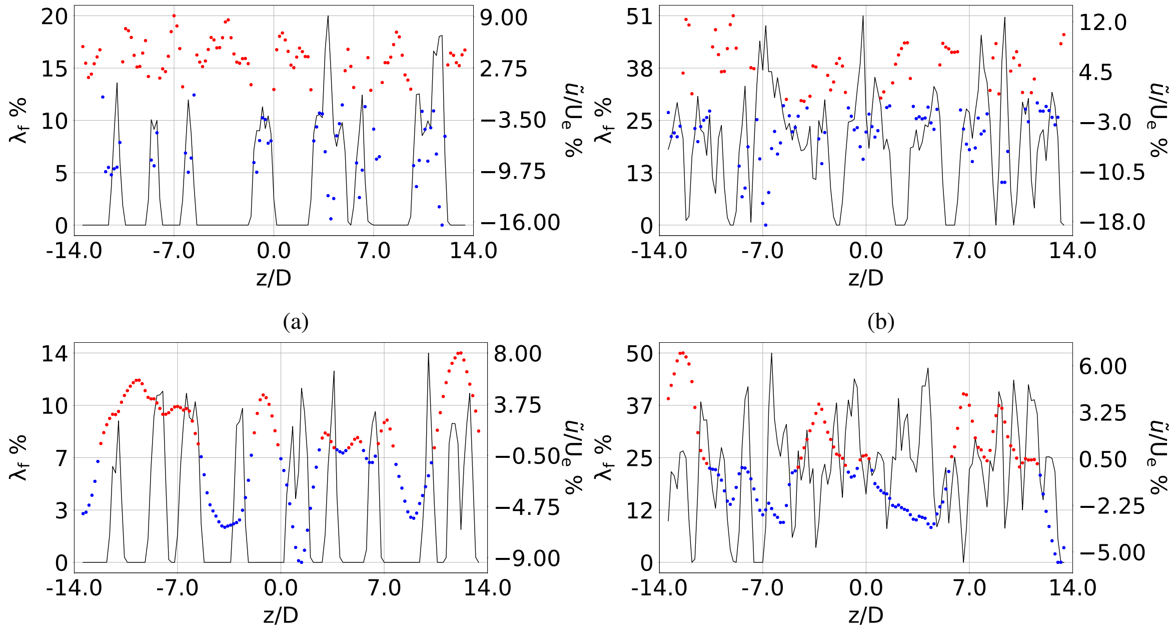

(a) (b) (c) (d)

Figure 6: Correlation of the momentum pathways with the topography underneath. —— Frontal area coverage, λ_f; • HMP; • LMP. (a) random topography (R10) at the leading of the roughness; (b) random topography (R57) at the leading of the roughness; (c) random topography (R10) at $x/D = 110$; (d) random topography (R58) at $x/D = 110$.

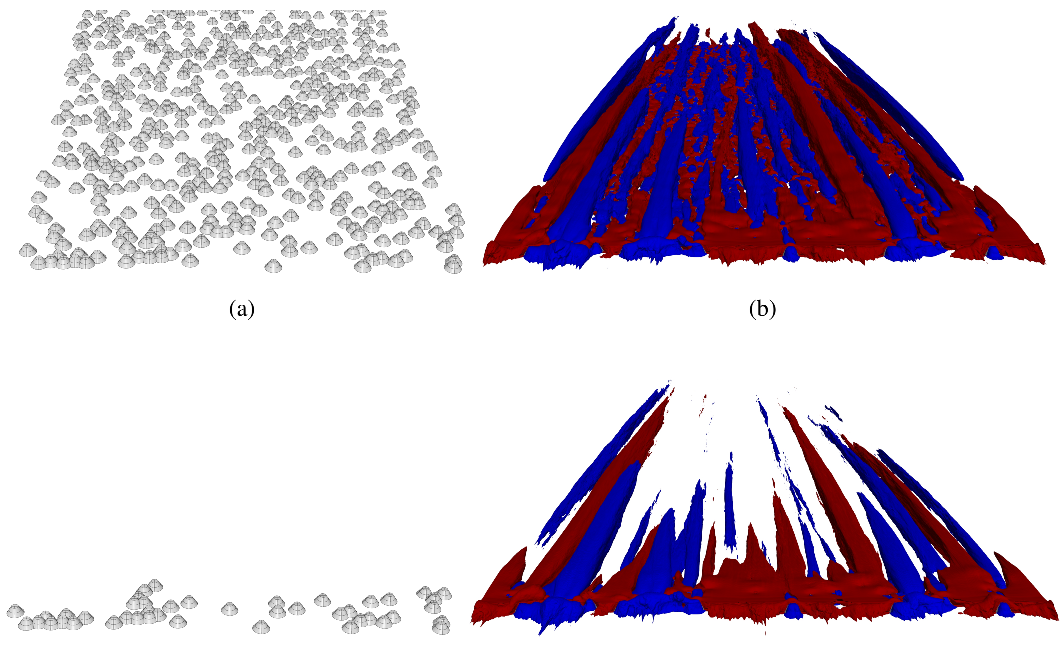

(a) (b) (c) (d)

Figure 7: Frontal view of (a) the original random, R39 topography configuration, (c) the LE of the roughness only. Isosurfaces of the time-averaged spanwise fluctuations of the streamwise velocity for the values of $\tilde{u}/U_e = 5\%$ HMP —— and $\tilde{u}/U_e = -5\%$ LMP —— in the case of the random, R39 topography; for (b) the original arrangement. (d) the LE of the roughness only.

though the strength of the momentum pathways seems to be affected by the absence of the downstream topography, their streamwise coherence is still significant and extends through the whole roughness domain (i.e. $60\delta_o$, where δ_o is the incoming boundary layer thickness). Furthermore, the streamwise coherence of the momentum pathways observed in the original arrangement can be found in the current modified case exactly the same in lower strength values (e.g. $|\tilde{u}/U_e| \approx 2\%$). The latter observations strongly contribute to the idea that the observed momentum pathways are entirely defined by the very upwind part of the roughness and that the downstream topography may slightly affect their strength.

The impact of these secondary flows on the structure of the boundary layer over a rough wall remains an open question. Womack *et al.* (2022), for example, observed heterogeneity among the mean streamwise velocity profiles along the spanwise direction highlighting the effect of the secondary flows in the mean flow statistics. They noted that the biggest deviation occurs in the random arrangements, while quick convergence within one roughness height, k, above the roughness crest was detected in the case of staggered arrangements. The same behaviour is observed in the DNS reported here. Mean velocity profiles at the same streamwise location and Reynolds number, are shown in Figure 8 for the cases of the staggered (S39) and random (R10 and R57) arrangements. The velocity profiles for the staggered arrangement (Figure 8a) show very small deviation with this scaling, while significant difference almost across the whole boundary layer height is observed for the random arrangements (Figure 8b-c). This is an indication that the outer-layer similarity breaks down in these cases, and the strong secondary motions are the primary contributor.

Summary and Conclusions

We present DNS of a zero pressure gradient boundary layer evolving over different configurations of truncated cones. Excellent agreement is achieved for the flow statistics compared to the experimental work by Womack *et al.* (2022). Presence of significant and coherent secondary flows due to roughness irregularity is demonstrated for the cases with random topographies. The lateral momentum transfer mechanism between the momentum pathways is investigated and attributed to counter-rotating vortices lying in the base of the HMP. Correlation of the locations of the HMP and LMP with the lower and higher values of the surface statistics respectively in the leading edge of the roughness is demonstrated. This correlation is very weak further downstream.

REFERENCES

Barros, J. M. & Christensen, K. T. 2014 Observations of turbulent secondary flows in a rough-wall boundary layer. *J. Fluid Mech.* **748**, R1.

Mejia-Alvarez, R & Christensen, K. T. 2013 Wall-parallel stereo particle-image velocimetry measurements in the roughness sublayer of turbulent flow overlying highly irregular roughness. *Physics of Fluids* **25**, 129901.

Womack, K. M., Volino, R. J., Meneveau, C. & Schultz, M. P. 2022 Turbulent boundary layer flow over regularly and irregularly arranged truncated cone surfaces. *J. Fluid Mech.* **933**, A38.

Yang, Jianming & Balaras, Elias 2006 An embedded-boundary formulation for large-eddy simulation of turbulent flows interacting with moving boundaries. *J. Comput. Phys* **215** (1), 12–40.

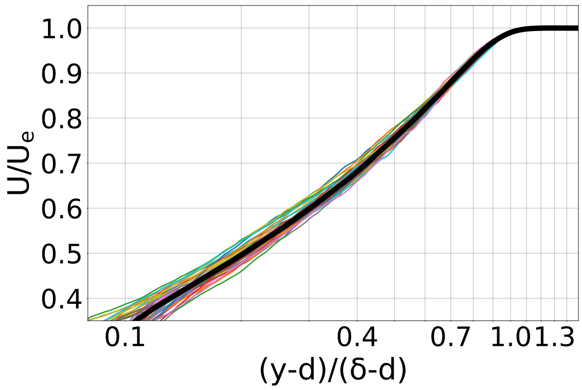

(a)

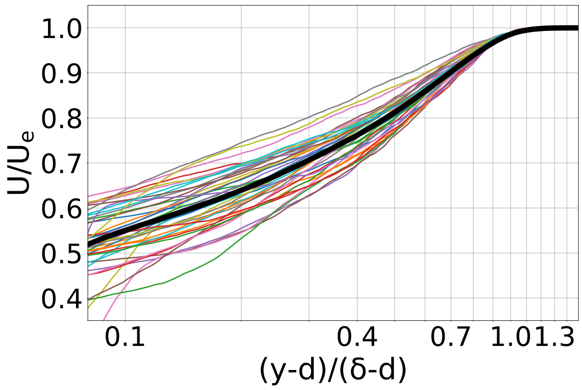

(b)

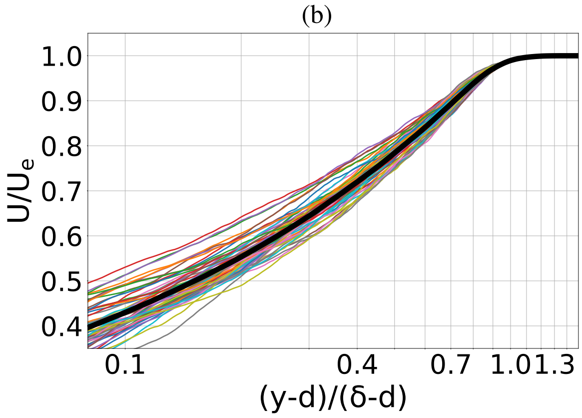

(c)

Figure 8: Mean streamwise velocity profiles in outer coordinates at $x/D = 110$ for various spanwise coordinates. (a) staggered topography (S39); (b) random topography (R10); (c) random topography (R57). ▬ represents the spanwise-averaged velocity profile.